Volume 1 | Number 1 | Jan 2013 | Pages 1–100

Journal of
Materials Chemistry A

Materials for energy and sustainability
www.rsc.org/materialsA

Li⁺

e⁻

Li⁺

e⁻

e⁻

Li⁺

Li⁺

ROYAL SOCIETY
OF CHEMISTRY

ROYAL SOCIETY
OF CHEMISTRY

www.rsc.org/materialsA

Journal of Materials Chemistry A

ARTICLE

From kröhnkite- to alluaudite-type of structure: novel method of synthesis of sodium manganese sulfates with electrochemical properties in alkaline ion batteries

D. Marinova,[a] V. Kostov,[b] R. Nikolova,[b] R. Kukeva,[a] E. Zhecheva,[a] M. Sendova-Vasileva,[c] and R. Stoyanova[a] *

The alluaudite-type of structure is of huge research interest as an open matrix ensuring fast alkaline ion mobility, a property that could contribute to the development of novel electrode materials for rechargeable alkaline ion batteries. In this contribution, we provide new data on the formation of well-crystallized sodium manganese sulfates $Na_{2+\delta}Mn_{2-\delta/2}(SO_4)_3$ with an alluaudite-type of structure by simple dehydratation of the corresponding dihydrate $Na_2Mn(SO_4)_3 \cdot 2H_2O$ with a kröhnkite-type of structure. The structure of $Na_{2+\delta}Mn_{2-\delta/2}(SO_4)_3$ is determined on the basis of Rietveld refinement of powder XRD patterns, infrared (IR) and Raman spectroscopy and electron paramagnetic resonance at X- and Q-band frequencies (EPR). From a structural point of view, the release of two H_2O molecule from the kröhnkite phase takes place by a transformation of the infinite $[Mn(SO_4)_2(H_2O)_2]$ chains into Mn_2O_{10} dimers bounded by distorted Na(1)O-polyhedra. The anhydrous sulfates are able to participate in the electrochemical reaction delivering reversible capacity of 135 mAh/g, when they are used as cathode materials in lithium ion cells. The stability of the alluaudite phase $Na_{2+\delta}Mn_{2-\delta/2}(SO_4)_3$ in the lithium electrolyte solution and the mechanism of the electrochemical reaction are discussed on the basis of *ex-situ* EPR, IR and Raman spectroscopy. This is a first report on electrochemical activity of manganese-based sulfate with an alluaudite-type of structure.

Introduction

Polyanion-based electrode materials for lithium ion batteries are designed to respond, to a great extent to the modern requirements for safety, durability and environmental compatibility.[1] From the first report on electrochemical properties of lithium iron phospho-olivine $LiFePO_4$ in 1997 till now, there is a challenging research competition aimed at defining the most suitable polyanion-structure matrix for reversible and fast lithium intercalation.[1-3] As a result, several groups of compounds including phosphate, silicates, sulfates, borates and mixed oxy-, hydroxy-, fluoro-phosphates and sulfates have been proposed for this purpose.[1] The common feature of all polyanion-based compounds is the building up of a stable three-dimensional framework by developing variety of bonds between transition metal ions and polyanions $(XO_4)^{n-3}$. Therefore, polyanion-based compounds represent a diversity

of structures all of which are able to intercalate lithium ions quickly and reversibly: olivine-, tavorite-, triplite-, silimanite-, marinate-type of structures.[1] Recently, the research interest has been focused on the alluaudite-type of structure.[1,4-8] The alluaudite phase with a general formula $A(2)A(1)M(1)M(2)_2(XO_4)_3$ has been first reported for natural minerals,[9,10] as well as for synthetic phases based on phosphates, molybdates and arsenates.[5,11] Very recently, synthetic sulfates of sodium-iron and sodium-manganese have been found out to crystallize in an alluaudite-type of structure too.[6-8] These compounds with a general composition $Na_{2+\delta}M_{2-\delta/2}(SO_4)_3$ (M ≡ Fe and Mn) have been classified as new type of insertion electrodes [6-8] and the electrochemical activity of iron analogue have been examined in model sodium ion cells.[6] Both lithium and sodium batteries operate via the same mechanism, involving a reversible solid state transfer of Li^+ or Na^+ between anodes and cathodes.[12] The sodium ion batteries have been designed as a low cost alternative to the present-day lithium ion batteries due to the high abundance and lower price of sodium in comparison with lithium.[12,13]

Sulfate-based polyanion compounds attract recently a huge research interest as electrode materials. Lithium iron sulfate $Li_2Fe(SO_4)_2$ is able to intercalate Li^+ at a potential higher than that for a fuorine-free iron-based compound.[14] Hydrated double salts with a kröhnkite-type structure display a good electrochemical performance in both lithium and sodium ion batteries.[15,16] For example, superior intercalation of both Na^+

[a.] *Institute of General and Inorganic Chemistry, Bulgarian Academy of Sciences 1113 Sofia, Bulgaria.*
[b.] *Institute of Mineralogy and Crystallography, Bulgarian Academy of Sciences, 1113 Sofia, Bulgaria.*
[c.] *Central Laboratory of Solar Energy and New Energy Sources, Bulgarian Academy of Sciences, Sofia, Bulgaria.*
* Corresponding author: radstoy@svr.igic.bas.bg

and Li$^+$ has been established for the composite Na$_2$Fe(SO$_4$)$_2$·2H$_2$O-graphene with a sandwich-type structure.[16] While most of the studies are directed to synthesis, structural characterization and electrochemistry of iron-based compounds, the manganese-based compounds are only sporadically examined. In comparison to iron-based compounds, the manganese ones appear to be more promising since they offer a higher potential of Li$^+$ intercalation (i.e. 4.1 V versus 3.5 V for the phospho-olivine phase, respectively), as a result of which a higher theoretical energy density can be achieved with them.[17] However, the preparation of manganese-based compounds as electrochemically active materials is a difficult task due to their lower electronic conductivity and greater lattice distortion degree due to the Jahn-Teller's instability of Mn^{3+} ions.[18,19]

In this contribution, we provide new data on the formation of well-crystallized sodium manganese sulfates Na$_{2+\delta}$Mn$_{2-\delta/2}$(SO$_4$)$_3$ with an alluaudite-type of structure by simple dehydratation of the corresponding dihydrate Na$_2$Mn(SO$_4$)$_3$·2H$_2$O with a kröhnkite-type of structure. The crystalline structure and the surface morphology of sodium manganese sulfates were analyzed by means of X-ray powder diffraction, SEM, IR and Raman spectroscopy and electron paramagnetic resonance spectroscopy (EPR). The anhydrous sulfates are able to participate in the electrochemical reaction by delivering capacity of 135 mAh/g, when they are used as cathode materials in lithium ion cells. The intercalation properties of anhydrous double sulfates were tested in model lithium cells versus lithium anode. Prior to the electrochemical test, the stability of anhydrous double sulfates in the lithium electrolyte had been studied by soaking them in the solution of LiPF$_6$ in EC:DMC. The structural changes during electrochemical reaction are monitored by ex-situ XRD, EPR, IR and Raman spectroscopy. This is the first report on the electrochemical activity of manganese-based alluaudite-phase. The mechanism of the electrochemical reaction is discussed on the basis of ex-situ electron paramagnetic resonance (EPR) and Raman spectroscopy.

Experimental

The Na$_2$Mn(SO$_4$)$_2$·2H$_2$O was prepared according to the solubility diagram of the three component Na$_2$SO$_4$ – MnSO$_4$ – H$_2$O system at 25°C using the method of isothermal decrease in super-saturation.[20] The completely anhydrous compound was obtained by heating at 227°C for one hour in argon flow. All the reagents used were "p.a." quality (Merck).

A Thermo SOLAAR M5 flame atomic absorption spectrometer with deuterium background corrector was used in this study. All measurements were performed in air-acetylene flame under standard conditions.

The X-ray powder diffraction spectra were collected within the range from 5° to 70° 2θ with a scanning step 0.02° 2θ and counting time 1s/step on Bruker D8 Advance diffractometer with CuKα radiation and LynxEye detector. The Rietveld refinement procedure is carried out with the GSAS program and EXPGUI.[21,22] A search was undertaken in ICDD 4.14.0.6

database (PDF-4+ 2014 RDB 4.1403)[23] using chemical criterion for the strongest line.

The DTA/TG curves of samples were measured using LABSYS™ EVO (Setaram, France) apparatus in a temperature range of 30–400 °C at a heating rate of 5 °C min^{-1} in air atmosphere.

The infrared spectra were recorded on a Nicolet iS5 Fourier transform interferometer (resolution < 2 cm^{-1}) at ambient temperatures using KBr discs as matrices. No ion exchange or other reactions with KBr have been observed.

The Raman spectra were recorded with a Horiba Jobin Yvon LabRAM HR800 spectrometer using the 600 l/mm grating and HeNe laser for excitation. The samples were placed under the 100X achromatic objective of a BX41 microscope and measured in back scattering configuration. The laser power on the sample was kept below 0.1 mW so that no heating effects on the powder sample could be observed.

The surface morphology of the samples was observed by JEOL JSM 6390 scanning electron microscope equipped with an energy dispersive X-ray spectroscopy (EDS, Oxford INCA Energy 350) in a regime of secondary electron image (SEI). The accelerating voltage was 20 kV and I ~ 65 µA. The pressure was of the order of 10^{-4} Pa. Before analysis the samples were metallized with gold.

The coordination of Mn ions in kröhnkite- and alluaudite phases was determined by a Bruker EMX^{plus} EPR spectrometer operating in the X-band (9.4 GHz) and the Q-band (34 GHz) in the temperature range of 100 – 500 K. It should be emphasized that for in-situ EPR experiments the temperature was raised in a step-like mode and, during the registration of EPR spectra at selected temperature, the temperature is retained for 3 min. This determines some changes in the temperature of dehydration determined from DTA/TG and EPR experiments.

The electrochemical charge-discharge curves of sodium manganese sulfates were examined by using Swagelok type two-electrode cells comprising Li|LiPF$_6$ (EC:DMC)| Na$_{2+\delta}$Mn$_{2-\delta/2}$(SO$_4$)$_3$. The positive electrode, supported on an aluminium foil, was a mixture containing 80% of the active Na$_{2+\delta}$Mn$_{2-\delta/2}$(SO$_4$)$_3$, 7.5% C-NERGY KS 6 L graphite (TIMCAL), 7.5% Super C65 (TIMCAL) and 5% polyvinylidene fluoride (PVDF). The loaded mass of active materials on Al collectors was about 4 mg. The electrolyte was a 1M LiPF$_6$ solution in ethylene carbonate and dimethyl carbonate (1:1 by volume) with less than 20 ppm of water. The lithium electrodes consisted of a clean lithium metal disk with diameter of 10 mm. The cells were mounted in a dry box under argon atmosphere. The electrochemical reactions were carried out using an eight-channel Arbin BT2000 system in galvanostatic mode. The charge and discharge rates were expressed as C/h, where h is the time interval in hours, needed for the insertion of one lithium ion per formula unit at the applied current intensity. The model lithium cell was cycled between 4.70 and 2.00 V at C/20, C/25 and C/100 rates.

The stability of sodium manganese sulfates in the lithium electrolyte was tested by soaking anhydrous Na$_{2+\delta}$Mn$_{2-\delta/2}$(SO$_4$)$_3$ in the solution of LiPF$_6$ salt in EC:DMC for 14 days. All the

experiments were carried out in dry box. After soaking the sample $Na_{2+\delta}Mn_{2-\delta/2}(SO_4)_3$ was washed with acetone and then dried on pieces of filter paper for 24 h in the dry box. The so treated samples were subjected for XRD and EPR experiments. The structural changes of electrode samples during electrochemical reaction were analyzed using lithium half-cells stopped at selected potentials. The electrochemical cells were disassembled insight a glove-box, followed by removing and washing of the working electrodes with EC. The quartz tube was filled with electrodes inside the glove-box for the EPR experiments.

Result and Discussion

Thermal dehydratation of $Na_2Mn(SO_4)_2 \cdot 2H_2O$

The crystallization of Na_2SO_4 and $MnSO_4$ salts from water solution yields single phase $Na_2Mn(SO_4)_2 \cdot 2H_2O$ with a kröhnkite-type of structure (Fig. 1). The chemical analysis confirms that the ratio between Na and Mn is 2:1 in the crystallized double sulfate salt. The lattice parameters of $Na_2Mn(SO_4)_2 \cdot 2H_2O$ are a = 5,8206±0.0002, b = 12,9958±0.0021, c = 5,4920±0.0018 Å, β = 106,10±0.04°, V = 399.1 Å^3 (space group $P2_1/c$). It is noticeable that the lattice parameters are in good agreement with those determined previously with a single crystal: a = 5.824(1), b = 12.999(1), c = 5.497(1) Å, β = 106.05(1)°, V = 399.9 Å^3.[24] The $Na_2Mn(SO_4)_2 \cdot 2H_2O$ phase is isostructural to iron compound $Na_2Fe(SO_4)_2 \cdot 2H_2O$.[15] In comparison with iron analogue $Na_2Fe(SO_4)_2 \cdot 2H_2O$, the lattice cell volume of $Na_2Mn(SO_4)_2 \cdot 2H_2O$ is higher (399.1 versus 391.8 Å^3, respectively), which matches the difference between ionic radii of Mn^{2+} and Fe^{2+} (0.83 Å versus 0.78 Å, respectively). The structure of the kröhnkite is composed of infinite $[Mn(SO_4)_2(H_2O)_2]$ chains, which are built up from alternating vertex sharing SO_4 tetrahedra and MnO_6 octahedra running in parallel to [001] (Fig. 2).[25] The chain length (expressed by c parameter) is strongly increased when going from Fe^{2+} to Mn^{2+} ions: c=5.44923 [15] versus c=5.492 Å. The chains are linked into layers by Na^+ ions coordinated by O^{2-} ions and by the hydrogen bonds. The distance between neighboring $[Mn(SO_4)_2(H_2O)_2]$ chains within a layer (expressed by a-parameter) is also affected by the presence of either Fe or Mn ions: a=5.76386 Å versus a=5.821 Å. The only parameter that seems to be unaffected by transition metal ions is the distance between the layers (expressed by $b/2$): b=12.97517 versus b=12.996 Å.

Although the single kröhnkite phase $Na_2Mn(SO_4)_2 \cdot 2H_2O$ crystallizes at room temperature from water solution of Na_2SO_4 and $MnSO_4$, the iron analogue $Na_2Fe(SO_4)_2 \cdot 2H_2O$ containing impurity of bloedite $Na_2Fe(SO_4)_2 \cdot 4H_2O$ (i.e. about 14.42 wt%) is obtained by the classical dissolution and precipitation route at 70-80 ^{o}C.[15] The advantage of our method of preparation is also demonstrated by the SEM study of morphology of the kröhnkite phase $Na_2Mn(SO_4)_2 \cdot 2H_2O$ (Fig. 3). The SEM micrographs are showing that $Na_2Mn(SO_4)_2 \cdot 2H_2O$ consists of well-faceted particles having polygon shapes and sizes between 1 and 5 μm.
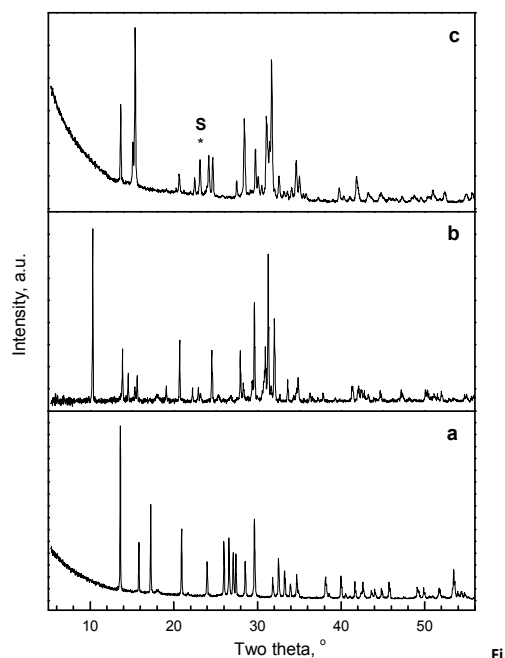
Figure 1. Powder XRD patterns of the kröhnkite phase Na2Mn(SO4)2·2H2O (a) and its partially (b) and completely (c) dehydrated products obtained at 162 and 230 oC, respectively (* – peak of orthorhombic sulfur)
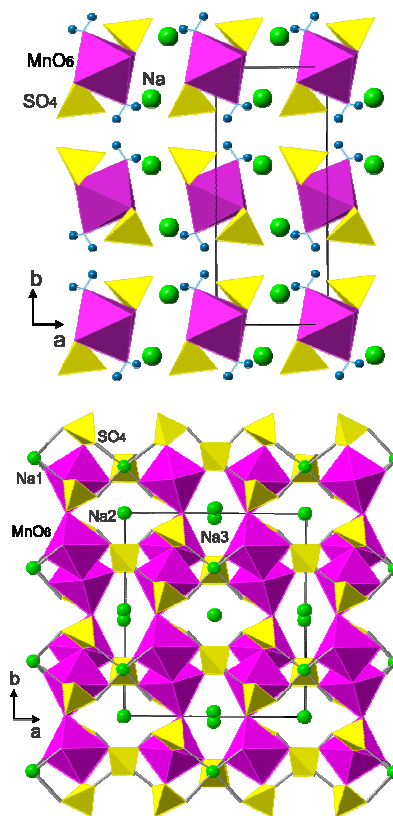

Figure 2. General view of the kröhnkite- and alluaudite-type structures (top and bottom).

The kröhnkite phase $Na_2Mn(SO_4)_2 \cdot 2H_2O$ is stable up to 130°C (Fig. 4). Above 130°C, $Na_2Mn(SO_4)_2 \cdot 2H_2O$ is decomposing in two distinct steps: between 135 °C and 193°C, there is a loss of one water molecule (5.46 wt % versus calculated one 5.48 wt%), followed between 203 °C and 289°C with a loss of the second water molecule (6.48 wt % versus calculated one 5.48 wt%). The XRD patterns of partially and completely dehydrated products show that the dehydration process occurs via a phase trasformation (Fig. 1).

The thermal dehydration process is interpreted in terms of manganese coordination by *in-situ* EPR spectroscopy at X-band frequency. The EPR spectra of $Na_2Mn(SO_4)_2 \cdot 2H_2O$ heated from 290K to 490K are shown in Figure 5. The kröhnkite phase $Na_2Mn(SO_4)_2 \cdot 2H_2O$ displays single Lorentzian line with *g*-factor of 2.015 and line width of 29 mT between 290K and 380K. These EPR parameters are consistent with a single type of coordination of Mn^{2+} in the kröhnkite phase: every Mn^{2+} ion is surrounded by 6 oxygen anion ligands, 4 of them belonging to four separate SO_4 groups and the remaining two – to the 2 H_2O molecules. The MnO_6 octahedra exhibit generally moderate
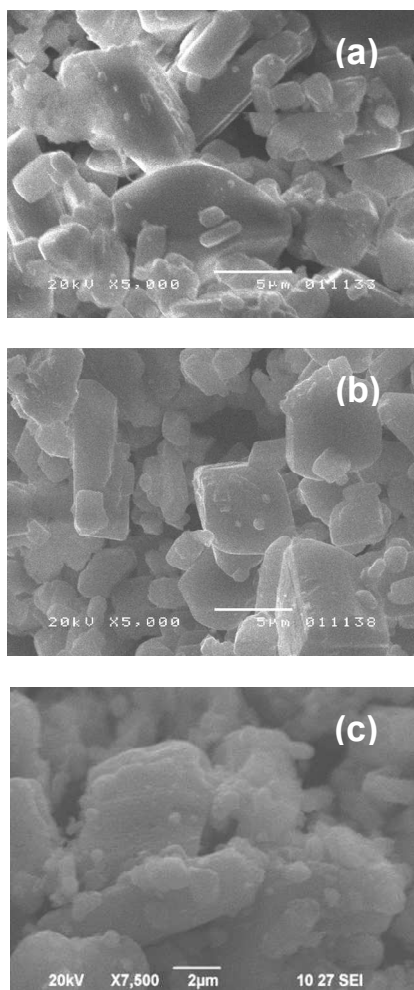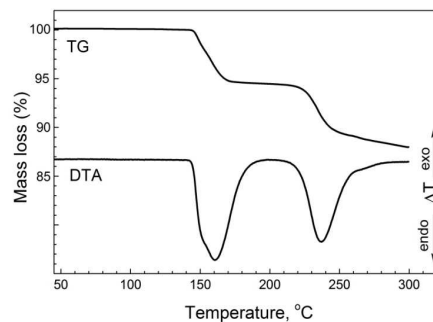
Figure 4 DTA/TG curves of $Na_2Mn(SO_4)_2 \cdot 2H_2O$

bond length (i.e. average Mn-O bond length of 2.191 Å) and weak bond angle distortion and they are connected via the SO_4 groups.[24] The appearance of one Lorentzian line originating from Mn^{2+} indicates that exchange interactions are occurring between them, which are able to smear the hyperfine structure due to nuclear spin of manganese atom (I=5/2).

The EPR signal of Mn^{2+} in $Na_2Mn(SO_4)_2 \cdot 2H_2O$ is observable between 290K and 380K. At temperature of 380K (107°C), the EPR spectrum undergoes a strong change (Fig. 5). The EPR spectrum is a convolution of two overlapping signals with Lorentzian shapes. The first signal exhibits a *g*-factor and line width that are close in value to those of the signal coming from kröhnkite phase $Na_2Mn(SO_4)_2 \cdot 2H_2O$. This means that the first signal is due to Mn^{2+} ions that have coordination similar to that of Mn^{2+} in $Na_2Mn(SO_4)_2 \cdot 2H_2O$. The second signal is extremely narrow (line width of about 9 mT) and it has a *g*-factor of 2.005. It is of importance that the g-value for the

Figure 3. SEM images of $Na_2Mn(SO_4)_2 \cdot 2H_2O$ (a); completely dehydrated products of $Na_2Mn(SO_4)_2 \cdot 2H_2O$ heated at 230 °C (b); $Na_{2+\delta}Mn_{2-\delta/2}(SO_4)_3$ soaked in the lithium electrolyte for 14 days (c).
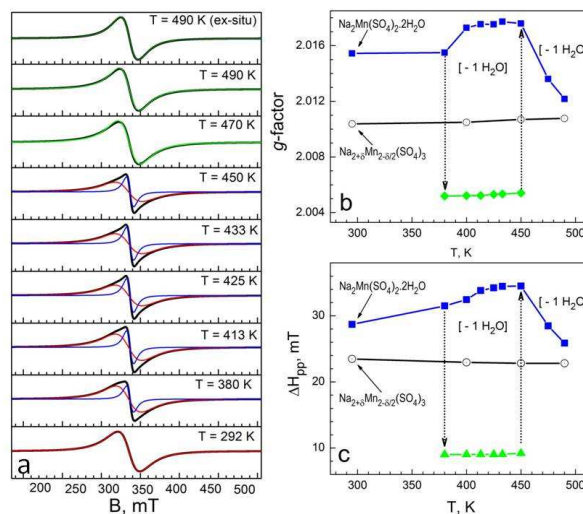
Figure 5. *in-situ* EPR spectra of $Na_2Mn(SO_4)_2 \cdot 2H_2O$ heated between 290 K and 490 K (a). The black lines correspond to the experimental spectra, while simulated signals due to Mn^{2+} ions are presented by red, blue and green lines. Temperature variation of the *g*-factors (b) and EPR line widths (c). For the sake of comparison, the *ex-situ* EPR spectrum and the temperature dependence of the *g*-factor and EPR line width for alluaudite $Na_{2+\delta}Mn_{2-\delta/2}(SO_4)_3$ obtained by heating of $Na_2Mn(SO_4)_2 \cdot 2H_2O$ at 230 °C are also given.

Journal Name   **ARTICLE**

second signal falls within the range, which is typical of Mn^{2+} ions. The second signal can also be associated with Mn^{2+} ions, but they have completely different coordination in comparison to Mn^{2+} in the kröhnkite phase. The difference is expressed by the number of SO_4 groups and H_2O molecules included in the first coordination sphere of Mn^{2+}. The splitting of the coordination of Mn^{2+} ions during heating reflects the thermal process, during which the first water molecule is being lost (Fig. 4).

The two overlapping signals give rise to the EPR profiles of $Na_2Mn(SO_4)_2 \cdot 2H_2O$ heated between 380K and 450K. In this temperature range, the g-factor and the line width of the broad signal are increasing, thus indicating a thermally induced deviation in the Mn^{2+} coordination mode from that in $Na_2Mn(SO_4)_2 \cdot 2H_2O$. Contrary to the broad signal, the narrow signal is retaining its g-factor and line width between 380K and 450 K. The relative intensity of the narrow signal increases, reaching a maximum of 11.5% at 433 K (i.e. 160 ^oC). It is worth mentioning that the narrow signal becomes more intensive at such temperatures, at which the peak maximum of the thermal loss of the first H_2O molecule is occurring. This supports once again that the release of the first H_2O molecule from $Na_2Mn(SO_4)_2 \cdot 2H_2O$ causes the splitting of Mn^{2+} coordination.

The EPR spectrum undergoes a further change above 450 K, where the second H_2O molecule is being released. The EPR spectrum consists of single Lorentzian line with a g-factor and a line width, which deviate significantly in comparison to those of the two types of Mn^{2+} ions (Fig. 5). This reveals a transformation from doubly coordinated into singly coordinated Mn^{2+} ions above 450 K. The EPR parameters of the new signal are also different from those of Mn^{2+} coordinated by 4 SO_4 groups and two H_2O molecules. Therefore, the new signal can be assigned to Mn^{2+} ions coordinated only by SO_4 groups. The XRD patterns of anhydrous sodium manganese sulfates shows that they crystallize in a structural type, which is different from that of the kröhnkite phase $Na_2Mn(SO_4)_2 \cdot 2H_2O$ (Fig. 1).

Combining DTA/TG, EPR and XRD data it appears that a dehydration of $Na_2Mn(SO_4)_2 \cdot 2H_2O$ is a complex process, which takes place in two stages via phase separation. The release of the first H_2O molecule causes a splitting in the Mn^{2+} coordination. This reflects, most probably, a phase separation process. After the loss of the second H_2O molecule, there is a subsequent phase transformation leading to the stabilization of single coordination of Mn^{2+} ions. The appearance of singly coordinated Mn^{2+} ions is associated with the formation of a new phase. The thermal dehydratation process of $Na_2Mn(SO_4)_2 \cdot 2H_2O$ can be understood on the basis of structural flexibility of the alkaline-oxygen polyhedron: the connectivity of NaO_x polyhedra can be described by forming corrugated network-like sheets parallel to (100). The channels running in parallel to (010) are the most favorable pathway for the Na^+ intercalation in the kröhnkite phase. The fast Na^+ mobility inside the kröhnkite phase $Na_2Mn(SO_4)_2 \cdot 2H_2O$ is a driving force to change the composition during the release of H_2O. The complexity in the thermal dehydration process has

also been established for the iron analogue,[15] where the anhydrous composition contains mainly thermodynamically stable $Na_6Fe(SO_4)_4$ impurity phase. The phase separation during the dehydration process is not a specific feature of the kröhnkite phase. Based on *in-situ* XRD experiments, it has been demonstrated that $Na_2Mn_{1.167}(SO_4)_2S_{0.33}O_{1.167} \cdot 2H_2O$ composition with a trigonal structure (space group R-3) is dehydrated in one single step by the formation of phase mixture between $Na_2Mn(SO_4)_2$ and MnS_2O_7.[26] All these data demonstrate occurring of a composition change during the dehydration process. The question is – what structural type and phase composition are stabilized during the dehydratation of the kröhnkite phase $Na_2Mn(SO_4)_2 \cdot 2H_2O$?

Crystalline Structure of $Na_2Mn_2(SO_4)_3$

Figure 6 gives the XRD pattern of the anhydrous sodium manganese sulfates. The XRD pattern is calculated within a structural model on the basis of an alluaudite-type of structure. The same structural type has been used to refine the structure of sodium-iron and sodium-manganese sulfates with composition $Na_{2+\delta}Fe/Mn_{2-\delta/2}(SO_4)_3$, where the Na-to-Mn ratio is lower than 2-to-1.[6,7,8] The formation of alluaudite phase from the kröhnkite phase $Na_2Mn(SO_4)_2 \cdot 2H_2O$ implies that the dehydration process takes place by changing the Mn-to-Na ratio.
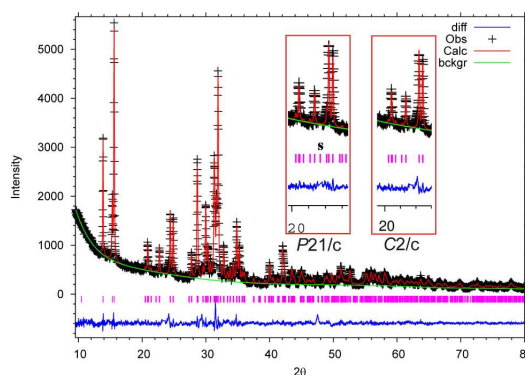
Figure 6 Rietveld refinement plot of $Na_{2+\delta}Mn_{2-\delta/2}(SO_4)_3$ calculated in the $C2/c$ space group. The crosses and continuous line correspond to the experimental and calculated XRD spectra. The Bragg's position below the excluded reflection is designated with the letter **s** in the insert.

For the iron analogue $Na_{2+\delta}Fe_{2-\delta/2}(SO_4)_3$, the structure has been described by two alternative models using space groups $P2_1/c$ (No. 14) and $C2/c$ (No. 15), respectively.[6] It is noticeable that the description in $P2_1/c$ is more reliable with respect to $Na_{2+\delta}Fe_{2-\delta/2}(SO_4)_3$,[6] while the model based on $C2/c$ is widely applied for the lattice description of all other alluaudite-phases.[9,10] Therefore, we calculated the structure of anhydrous sodium manganese sulfate $Na_{2+\delta}Mn_{2-\delta/2}(SO_4)_3$ within the framework of higher-symmetry structural model including space group $C2/c$. The structure was initially refined with soft constraints, consisting of all S-O bond distances and in the final refinement cycles they were released without causing any substantial structural distortions before reaching

convergence. All the atoms were refined isotropically. Expecting similar U_{iso} values for the O atoms these were refined in a group. The same approach was selected for the Mn atoms (for the primitive lattice case) and for the S atoms. Neutral atomic scattering factors, as these are stored in GSAS, were used for all atoms. No corrections were made for absorption.

Powder data statistics and crystallographic data from the refinement based on the $P2_1/c$ and $C2/c$ space group are represented in Table 1. The fractional atomic coordinates and thermal parameters for $Na_{2+\delta}Mn_{2-\delta/2}(SO_4)_3$ for the $C2/c$ model are listed in Table 2. Some selected interatomic distances for the $C2/c$ space group are shown in Table 3. In addition, the corresponding data for the lattice description in space group $P2_1/c$ are given in the supplementary information. As one can see, it is difficult to discriminate between the two structural models on the basis of powder data statistics only. The final difference plot of the X-ray Rietveld refinement in $C2/c$ space group is represented in Figure 6. Close inspection of the XRD pattern shows that the peak at $d=3.811$ Å cannot be fitted neither with $P2_1/c$ nor with $C2/c$ model. This peak can tentatively be ascribed to the orthorhombic sulfur (see files 01-078-8201, 00-042-1278, and 04-012-7312). Therefore, this peak is to be excluded from the refinement procedure (Fig. 6, insets). The inset, therein, presents the vicinity of the excluded

reflection in the 2θ° range and Bragg's position of the allowed reflection in $P2_1/c$ space group *(300)* below is designated by a letter **s** (Fig. 6). In comparison, this reflection is not allowed in the $C2/c$ space group.

The anhydrous compound $Na_{2+\delta}Mn_{2-\delta/2}(SO_4)_3$ is isostructural to $Na_2Fe_2(SO_4)_3$ (in $C2/c$ space group) and due to the difference in the ionic radii of Mn^{2+} and Fe^{2+} its unit cell volume is larger - 979.95(25) Å^3 *vs.* 949.86(11) Å^3 for the iron-containing phase.[6] The lattice volume of $Na_{2+\delta}Mn_{2-\delta/2}(SO_4)_3$, obtained from $Na_2Mn(SO_4)_2·2H_2O$, is slightly smaller than that reported for $Na_{2+\delta}Mn_{2-\delta/2}(SO_4)_3$ obtained by a solid state reaction [8] (i.e. 983.32(8) Å^3). However, it is worth mentioning that the goodness factor of fitting of the refined structure of $Na_{2+\delta}Mn_{2-\delta/2}(SO_4)_3$ studied by us is three-four times better than that reported by Barpanda *et al.* [8]. For the $C2/c$ model, the Mn ions occupy single crystallographic position. The crystallographically equivalent MnO_6 units are coupled by edge

Table 1. Crystallographic data and results of the Rietveld refinement of $Na_{2+\delta}Mn_{2-\delta/2}(SO_4)_3$

	1	2	3
Space group		$P2_1/c$	$C2/c$
Cell parameters:			
a (Å)		11.541(1)	12.764(1)
b (Å)		12.944(1)	12.943(1)
c (Å)		6.5875(6)	6.5871(6)
angles (°) ά		90.000	90.000
angles (°) β		95.149(3)	115.780(3)
angles (°) γ		90.000	90.000
V (Å^3)		980.13(26)	979.95(25)
Formula unit		$Na_{2.74}Mn_{1.86}(SO_4)_3$	$Na_{2.76}Mn_{1.78}(SO_4)_3$
Calculated unit cell Fw		1816.804	1803.574
Z		4	4
P_{calc} (g cm^{-3})		3.078	3.056
Wavelength (Å)		1.5419	1.5419
2θ range (deg)		9.5-80	9.5-80
Step-scan increment (2θ), deg		0.02	0.02
Step-scan time, s		35	35
No of data points		3555	3557
No of contributing reflections		1379	692
No of varied parameters		79	55
Profile function		Pseudo-Voight	Pseudo-Voight
R_{wp}		0.0649	0.0710
R_p		0.0478	0.0501
R_F^2		0.0520	0.0657
χ^2		1.939	2.305

Table 2. Fractional atomic coordinates, occupancies and isotropic displacement parameters for the $C2/c$ model of $Na_{2+\delta}Mn_{2-\delta/2}(SO_4)_3$.

| Atom	x	y	z	Occ.	B / Å2
Na1	0.5000	0.7296(7)	0.7500	1	1.81(33)
Na2	0.0000	0.0000	0.0000	0.839(13)	17.94(78)
Na3	0.5000	0. 9757(12)	0.2500	0.918(11)	10.07(56)
Mn	0.7269(5)	0.1561(4)	0.1422(9)	0.892(8)	4.42(16)
S1	0.0000(0)	0.7820(7)	0.7500(0)	1	2.06(16)
O11	0.0797(8)	0.8459(10)	0.7100(19)	1	1.517(16)
O12	0.4451(9)	0.2124(9)	0.5507(21)	1	=O11
S2	0.7647(6)	0.6105(5)	0.8661(11)	1	=S1
O21	0.7706(10)	0.6662(10)	0.6880(18)	1	=O11
O22	0.3190(9)	0.9928(11)	0.3704(19)	1	=O11
O23	0.3449(11)	0.5807(9)	0.6504(18)	1	=O11
O24	0.3362(10)	0.1581(8)	0.0901(22)	1	=O11

Table 3. Selected interatomic distances (Å) for the coordination polyhedra in the $C2/c$ model of $Na_{2+\delta}Mn_{2-\delta/2}(SO_4)_3$.

S1 – O11	1.422(11)	S2 – O21	1.406(12)		
– O11	1.422(11)	– O22	1.499(12)		
– O12	1.492(11)	– O23	1.409(10)		
– O12	1.492(11)	– O24	1.490(13)		
Na1 – O11	2.915(11)	Na2– O11	2.388(12)	Na3– O12	2.710(12)
– O11	2.915(11)	– O11	2.388(12)	– O12	2.710(12)
– O12	2.487(12)	– O23	2.520(12)	– O22	2.759(11)
– O12	2.487(12)	– O23	2.775(12)	– O22	2.759(11)
– O23	2.634(12)	– O23	2.520(12)	– O22	2.594(11)
– O23	2.634(12)	– O23	2.775(12)	– O22	2.594(11)
– O24	2.381(12)			– O24	3.023(11)
– O24	2.381(12)			– O24	3.023(11)
Mn – O11	2.224(9)				
– O12	2.131(11)				
– O21	2.355(13)				
– O21	2.193(11)				
– O22	2.186(14)				
– O24	2.236(11)				

sharing to form Mn_2O_{10} dimers, which are in their turn connected by SO_4 tetrahedra to form three-dimensional framework with cavities and channels (Fig. 2). The $Mn_{1.78}(SO_4)_3$ framework carries negative charge, whose compensation is achieved through the sodium ions. The latter occupy three symmetrically independent positions. One of them resides in the cavities connected in a very narrow channel running along a axis. The channels running along c axis are more interesting, where the rest of the charge compensating ions are located. As it is discussed previously [6,7] their effective diameter is suitable for fast Na^+ diffusion during electrode reaction. The Na motion pathways for both types of channels are represented in Figure 7. The measured O–O distances characterizing the effective pore size of the channels exhibit slightly larger values in comparison to those ones in the Fe structural analogue. This will ensure a faster mobility of Na^+ in the manganese analogue.

IR and Raman methods have been applied to elucidate the structure. For the lattice description in $C2/c$ space group, S
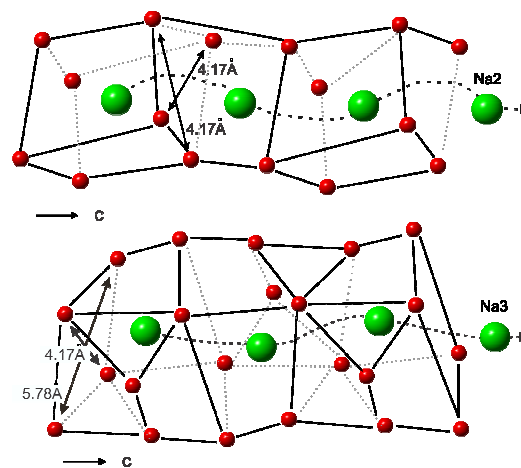
Figure 7 Na2 and Na3 motion pathways inside a channel running along the c axes.

atoms occupy two crystallographically non-equivalent positions, while three positions are available for S atoms in the $P2_1/c$ model. The analysis of the IR and Raman spectra of alluaudite phase is based on the comparison with corresponding spectra of the kröhnkite phase. The free sulfate groups (SO_4^{2-}) under perfect T_d symmetry exhibit four internal vibrations: $\nu_1(A_1)$, the symmetric S–O stretching mode, $\nu_2(E)$, the symmetric SO_4 bending modes, $\nu_3(F_2)$ and $\nu_4(F_2)$, the asymmetric S–O stretching and SO_4 bending modes, respectively. The normal vibrations of free SO_4^{2-} ions in aqueous solution appear at $\nu_1 = 983$ cm^{-1}, $\nu_2 = 450$ cm^{-1}, $\nu_3 = 1105$ cm^{-1} and $\nu_4 = 611$ cm^{-1}.[27] Transferring into solid state, the vibration spectra of SO_4^{2-} become more complicated. The factor group analysis for the SO_4 groups in the kröhnkite-type of structure for $Na_2Mn(SO_4)_2 \cdot 2H_2O$ predicts that in C_1 site symmetry under C_{2h} factor group symmetry the degeneracy of E and F_2 modes is removed, thus resulting in the appearance of two bands for ν_2 and three bands for ν_3 and ν_4 (all belonging to A symmetry). Due to the low site symmetry of the SO_4 tetrahedra the ν_1 mode is activated (A symmetry). Each internal mode could split additionally into four components $A_g+A_u+B_g+B_u$ (A_u and B_u are IR active, while Raman active are A_g and B_g). Therefore, six bands corresponding to the asymmetric stretches and two bands corresponding to the symmetric stretches are to be expected to appear in the IR spectrum of the monoclinic double salt.

Figure 8 compares the IR and Raman spectra of the kröhnkite phase $Na_2Mn(SO_4)_2 \cdot 2H_2O$ and of the anhydrous alluaudite phase $Na_{2+\delta}Mn_{2-\delta/2}(SO_4)_3$ in the vicinity of the SO_4^{2-} vibrations. The IR spectra are less resolved in comparison to the Raman spectra. This is an expected in advance result, if we take into account that the unit-cell group modes of SO_4 groups exhibit usually relatively large half-widths due to the LO/TO splitting of the corresponding bands with high oscillatory strength.[28] However, a series of bands are clearly resolved for the kröhnkite phase $Na_2Mn(SO_4)_2 \cdot 2H_2O$. The bands at 1192, 1146, 1097, 1079 and 1063 cm^{-1} appear within the range, where the ν_3 mode is active, while the symmetric and asymmetric bending modes (i.e. ν_2 and ν_4 modes) are associated with bands at 472 and 456 cm^{-1} and also at 646, 630, 607 and 582 cm^{-1}, respectively. The ν_1 mode is separated considerably from the ν_3 modes and it appears at lower frequencies as a single band at 985 cm^{-1}. The assignment of the IR bands is further confirmed by the analysis of the Raman spectrum. The Raman spectrum is dominated by a strong intensive band at 988 cm^{-1}, which indicates that this band arises from ν_1 mode. The ν_2, ν_3 and ν_4 modes are clearly manifested in the range of 440-470, 1020-1170 and 615-650 cm^{-1}, the band positions are summarized in Table 4. The broad band at about 850 cm^{-1} in the IR spectrum can be attributed to a water molecule librational mode.

In comparison with the kröhnkite phase $Na_2Mn(SO_4)_2 \cdot 2H_2O$, both the IR and Raman spectra are less resolved for the anhydrous alluaudite phase $Na_{2+\delta}Mn_{2-\delta/2}(SO_4)_3$. However, in the vicinity of the ν_3 mode, the IR
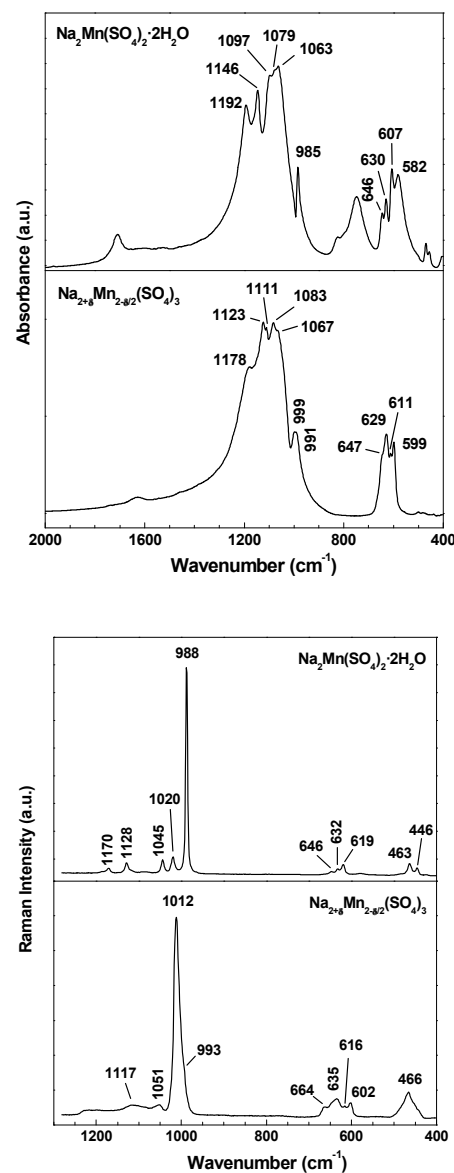
Figure 8 IR (top) and Raman (bottom) spectra of the kröhnkite phase $Na_2Mn(SO_4)_2 \cdot 2H_2O$ and of the anhydrous alluaudite phase $Na_{2+\delta}Mn_{2-\delta/2}(SO_4)_3$.

spectrum displays five bands, whose positions are close to that of SO_4^{2-} in kröhnkite phase (Table 4). The good similarity is also observed in the range of the ν_4 mode (Fig. 8, Table 4). The ν_2 mode exhibits only one broad band in the IR and Raman spectra. The main difference between the two phases is visible in the range of the ν_1 mode: the band becomes broader and it is shifted from 985 to 999 cm^{-1} for alluaudite $Na_{2+\delta}Mn_{2-\delta/2}(SO_4)_3$. In addition, the ν_1-band shows some asymmetry, as a result of which a new peak on the low wave-number side can be resolved (Fig. 8, Table 4). It is noticeable that both Raman and IR spectra display an asymmetry of the ν_1-band.

Table 4 Assignment of vibrational modes of SO_4^{2-} groups in $Na_2Mn(SO_4)_2 \cdot 2H_2O$ and $Na_{2+\delta}Mn_{2-\delta/2}(SO_4)_3$.

Vibrational mode	$Na_2Mn(SO_4)_2 \cdot 2H_2O$		$Na_{2+\delta}Mn_{2-\delta/2}(SO_4)_3$	
	IR spectra	Raman spectra	IR spectra	Raman spectra
v_1	985	988	999 / 991	1012 / 993
v_2	472	463	~ 450	~ 466
	456	446		
v_3	1192	1170	1178	~ 1220
	1146	1128	1123	
	1097		1111	1117
	1079	1045	1083	
	1063	1020	1067	1051
v_4	646	646	647	664
	630	632	629	635
	607	619	611	616
	582		599	602

The comparison of the vibrational spectra of $Na_2Mn(SO_4)_2 \cdot 2H_2O$ and $Na_{2+\delta}Mn_{2-\delta/2}(SO_4)_3$ evidences a similarity in the S coordination type in both structures. The observed shift of the symmetric S−O stretching vibration of SO_4 (i.e. v_1-mode) from the kröhnkite to the alluaudite phase implies that the S−O bond length becomes smaller: for $Na_2Mn(SO_4)_2 \cdot 2H_2O$ the mean S−O bond length is 1.479 Å, while only in the case of $Na_{2+\delta}Mn_{2-\delta/2}(SO_4)_3$ in $C2/c$ space group the S−O bond length is smaller (1.454 Å, Table 3). In the case of $P2_1/c$ model, the mean S−O bond length is larger (1.502 Å). All vibrational observations lead to the conclusion that the $C2/c$ model for description of structure of $Na_{2+\delta}Mn_{2-\delta/2}(SO_4)_3$ is more reliable, irrespective of the slightly better statistical data for the refinement of the structure in $P2_1/c$ model (Table 1).

The EPR spectroscopy in X- and Q-band frequency allows further discrimination between the two structural models for $Na_{2+\delta}Mn_{2-\delta/2}(SO_4)_3$. For the sake of comparison, we also studied the EPR spectra of $Na_2Mn(SO_4)_2 \cdot 2H_2O$. At room temperature the kröhnkite phase displays a single Lorentzian line at 9.4 and 34 GHz due to Mn^{2+} ions, coordinated by four SO_4 ions and two H_2O molecules. The frequency-independent g-value is 2.0003(4), while the EPR line width is slightly decreasing during the increasing of the microwave frequency: line width of 29.03(9) and 24.41(8) mT, when measured at 9.4 and 34 GHz, respectively. This means that the low-dimensional magnetic exchange interactions between Mn^{2+} ions contribute mainly to the EPR line shape. Upon cooling down from 290 to 100 K, the EPR signal intensity measured at 9.4 GHz is increasing following the Curie-Weiss law, the Weiss constant being -86 ± 9 K. The g-factor remains constant within the same temperature range, while the line width increases (Fig. 9). All these EPR parameters indicates that Mn^{2+} ions are coupled by magnetic exchange interactions inside the infinite $[Mn(SO_4)_2(H_2O)_2]$ chains. In addition, the contribution of some weak exchange interactions between the chains cannot be excluded. It is worth mentioning that the magnetic structure of the kröhnkite phase $Na_2Mn(SO_4)_2 \cdot 2H_2O$ has not been studied yet.

In comparison with the kröhnkite phase $Na_2Mn(SO_4)_2 \cdot 2H_2O$, the alluaudite phase $Na_{2+\delta}Mn_{2-\delta/2}(SO_4)_3$
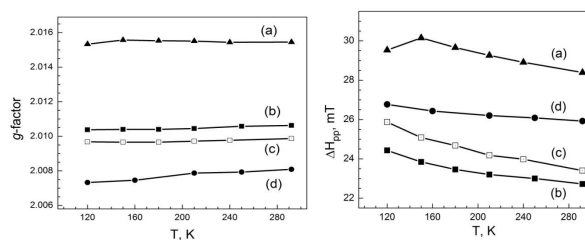
Figure 9 Temperature dependence of g-factor and EPR line width (ΔH_{pp}) of Mn^{2+} ions in: (a) $Na_2Mn(SO_4)_2 \cdot 2H_2O$; (b) anhydrous $Na_{2+\delta}Mn_{2-\delta/2}(SO_4)_3$; (c) $Na_{2+\delta}Mn_{2-\delta/2}(SO_4)_3$ after soaking for 14 days in the lithium electrolyte solution, and (d) $Na_{2+\delta}Mn_{2-\delta/2}(SO_4)_3$ after 10 cycles between 4.6 and 2.0 V (the cell is stop at 2.0 V).

exhibits also a single Lorentzian line in X- and Q-band frequency. The frequency-independent g-value is 2.0005(3) and it coincides with the g-value determined for the kröhnkite phase. This outlines that the EPR signal of $Na_{2+\delta}Mn_{2-\delta/2}(SO_4)_3$ is originating from Mn^{2+} ions too. The close values of g-factors for both kröhnkite and alluaudite phases can be related with the local geometry structure of Mn^{2+} ions environment: all Mn^{2+} are octahedrally coordinated with a mean Mn-O bond length of 2.197 and 2.221 Å, respectively (Table 4). In contrary with $Na_2Mn(SO_4)_2 \cdot 2H_2O$, the line width of $Na_{2+\delta}Mn_{2-\delta/2}(SO_4)_3$ does not show any dependence on the microwave frequency: 23.44(5) and 23.34(6) mT, when measured at 9.4 and 34 GHz, respectively. Moreover, the line width of Mn^{2+} in the alluaudite phase is slightly lower comparing with that for the kröhnkite phase. In the X-band frequency, the temperature dependence of the signal intensity obeys the Curie-Weiss law with a Weiss constant of -56 ± 7 K. It should be noted that $Na_{2+\delta}Mn_{2-\delta/2}(SO_4)_3$ obtained by a solid state reaction [8] displays a long range antiferromagnetic ordering at very low temperature of 3.4 K. Between 100 and 300 K, the g-factor of Mn^{2+} in $Na_{2+\delta}Mn_{2-\delta/2}(SO_4)_3$ remains constant, while the EPR line width is increased (Fig. 9). The lack of any dependence of the line width on the microwave frequency, as well as the magnitude of the Weiss constant, are an EPR evidence for the different magnetic structures of the kröhnkite and of the alluaudite phases. Although the magnetic structure of

$Na_2Mn(SO_4)_2 \cdot 2H_2O$ is a result from the exchange interactions inside infinite $[Mn(SO_4)_2(H_2O)_2]$ chains, the coupled MnO_6 units forming Mn_2O_{10} dimers give rise to the magnetic structure of anhydrous compound $Na_{2+\delta}Mn_{2-\delta/2}(SO_4)_3$. The Mn_2O_{10} dimers are linked by $Na(1)O$-polyhedra into infinite chains. The Na^+ ions directly bonded to Mn_2O_{10} dimers play a certain role to dilute the magnetic system, as a result of which the magnitude of the Weiss constant and the EPR line width become smaller in comparison with those of $Na_2Mn(SO_4)_2 \cdot 2H_2O$. On the other hand, the EPR spectroscopy does not provide any evidence for appearance of highly oxidized manganese ions (such as Mn^{3+} and/or Mn^{4+}) in the anhydrous compound. This supports the correctness of the used structural formula $Na_{2+\delta}Mn_{2-\delta/2}(SO_4)_3$.

Electrochemical properties of $Na_{2+\delta}Mn_{2-\delta/2}(SO_4)_3$

The availability of structural channels with a geometry ensuring fast Na^+ mobility makes the alluaudite phases very attractive as electrode materials for both lithium and sodium ion batteries.[7] First experimental reports have been focused on the electrochemical properties of phosphate-based compounds.[1,3] However, their electrochemical performance remains still unsatisfactory especially when the phosphate-based compounds are used as cathodes in sodium ion batteries. Delmas *et al.* have been proposed to test the alluaudite phase with a composition $NaMnFe_2(PO_4)_3$ as a cathode in an electrochemical cell versus lithium anode. It has been demonstrated that up to 1.5 Li^+ ions per formula unit could be intercalated during the first discharge with an average voltage around ~2.5V, while only 1.2 Li^+ could be extracted during the following charge.[5] Recently, Barpanda *et al.* have been found that sulfate-based compounds display much better electrochemical performance in comparison with the phosphate-analogues.[6] It is noticeable that most of studies deal with iron containing phases irrespective of the fact that the theoretical analysis predicts more challenging properties for the manganese containing compounds. Therefore, we examine the electrochemical properties of new synthesized manganese-based alluaudite phase $Na_{2+\delta}Mn_{2-\delta/2}(SO_4)_3$ in model lithium ion cells.

Prior to the electrochemical tests it is necessary to test the stability of $Na_{2+\delta}Mn_{2-\delta/2}(SO_4)_3$ phase in the lithium electrolyte. It has been accepted that $LiPF_6$ is a highly reactive reagent due to its thermal instability.[29] The $LiPF_6$ has been shown to decompose into LiF and PF_5 even at room temperature.[29] The reaction product PF_5 is a strong Lewis acid and it readily reacts with the surface of electrode materials leading to the formation of the solid-electrolyte inter-phase, containing a mixture of organic and inorganic compounds. Taking into account the possible interaction between double sulfates and lithium electrolyte, we studied the stability of the alluaudite phase in the lithium electrolyte by soaking of $Na_{2+\delta}Mn_{2-\delta/2}(SO_4)_3$ in the solution of $LiPF_6$ salt in EC/DMC solvent for 14 days. The soaked samples were then characterized by XRD, SEM, IR, Raman and EPR techniques.

The XRD patterns remain the same after the soaking of $Na_{2+\delta}Mn_{2-\delta/2}(SO_4)_3$ into electrolyte (not shown here). The

morphology of soaked $Na_{2+\delta}Mn_{2-\delta/2}(SO_4)_3$ is also preserved (Fig. 3). The Na-to-Mn ratio determined by Energy Dispersive X-ray (EDX) Spectroscopy is also constant: 11.77 and 5.74 atomic % for Na and Mn in the pristine composition versus 10.40 and 4.60 atomic % for Na and Mn in the soaked composition. This means that structure and morphology are stable after the contact of $Na_{2+\delta}Mn_{2-\delta/2}(SO_4)_3$ with lithium electrolyte.

The structure of SO_4 network is probed by IR and Raman spectroscopy (Fig. 10). As in the case of pristine $Na_{2+\delta}Mn_{2-\delta/2}(SO_4)_3$, the IR spectrum of soaked sample is dominated by the bands due to the v_3-vibration of SO_4 groups, while v_1- and v_4-vibrations cause the appearance of less intensive bands. (It should be recall that the v_2-mode is not well resolved in the IR spectrum of pristine $Na_{2+\delta}Mn_{2-\delta/2}(SO_4)_3$). All IR bands are split into several components, whose positions match well those for SO_4 groups in pristine $Na_{2+\delta}Mn_{2-\delta/2}(SO_4)_3$. The Raman spectrum of the soaked sample displays an intensive band with slight asymmetry at the low wave-number side. The same band is observed for pristine $Na_{2+\delta}Mn_{2-\delta/2}(SO_4)_3$ and it is attributed to the v_1-vibration of SO_4 groups. The comparison of IR and Raman spectra shows that the SO_4 network remains also unchanged during soaking of $Na_{2+\delta}Mn_{2-\delta/2}(SO_4)_3$ in the lithium electrolyte.
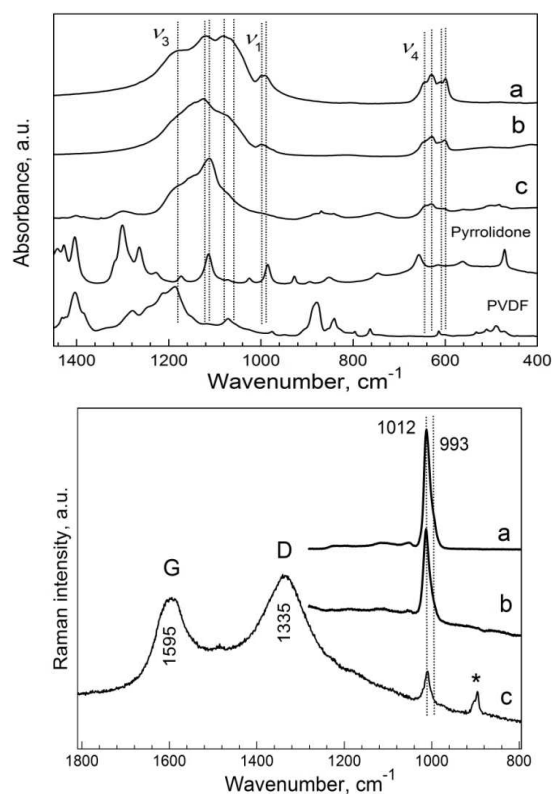
Figure 10. IR and Raman spectra of the alluaudite phase $Na_{2+\delta}Mn_{2-\delta/2}(SO_4)_3$: (a) pristine sample; (b) sample after soaking for 14 days in the lithium electrolyte solutions; (c) sample after 10 cycles between 4.6 and 2.0 V (the cell is stop at 2.0 V). For the sake of comparison, IR spectra of PVDF and pyrrolidone (used as bonding and dispersing agents in the electrode fabrication) are also given. The asterisk denotes the unknown Raman mode.

ARTICLE

The EPR spectroscopy confirms also the stability of the alluaudite phase $Na_{2+\delta}Mn_{2-\delta/2}(SO_4)_3$ in the lithium electrolyte solution (Fig. 9). The EPR spectrum consists of single Lorentzian line due to Mn^{2+} ions. Both the g-factor and the EPR line width measured between 100 and 300 K tend to that of the pristine sample $Na_{2+\delta}Mn_{2-\delta/2}(SO_4)_3$. Based on diffraction and spectroscopic techniques, one can conclude that $Na_{2+\delta}Mn_{2-\delta/2}(SO_4)_3$ is stable in the lithium electrolyte solution and it can be used as a cathode material.

Figure 11 shows the first charging/discharging curves of $Na_{2+\delta}Mn_{2-\delta/2}(SO_4)_3$. The cell starts with a charging mode, where Na^+ deintercalation from the alluaudite structure is to be expected to occur. The amount of intercalated alkaline ions is calculated on the basis of the structural formula derived from the Rietveld refinement: $Na_{2+\delta}Mn_{2-\delta/2}(SO_4)_3$ with $\delta=0.44$. In order to achieve a good electrochemical performance of $Na_{2+\delta}Mn_{2-\delta/2}(SO_4)_3$, we used the following electrochemical protocol: the first 9 cycles are performed by charging the electrochemical cell up to 4.70 V with a rate of C/25, keeping the voltage constant at 4.70 V for 5 hours, followed by a discharge mode with a rate of C/100. After these 9 cycles, the electrochemical cell is charged and discharged with a rate of C/100 between 4.6 and 2.0 V.
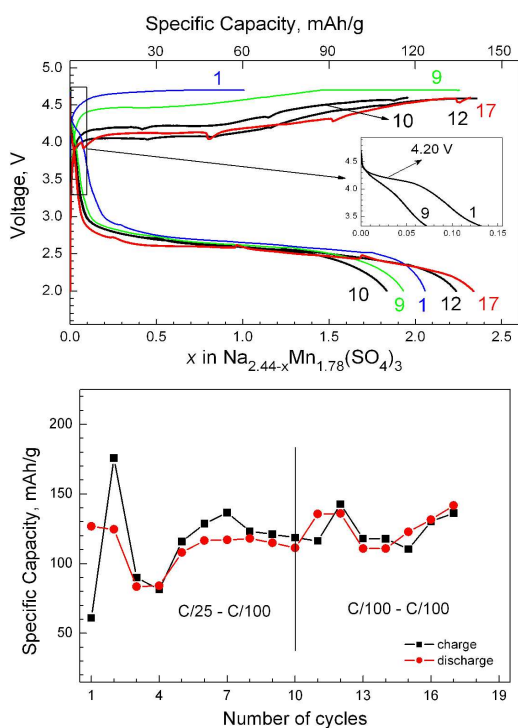

Figure 11 Charging/discharging curves for $Na_{2+\delta}Mn_{2-\delta/2}(SO_4)_3$ used as electrodes in model lithium cells (top). The charge/discharge cycling stability curves for $Na_{2+\delta}Mn_{2-\delta/2}(SO_4)_3$ (bottom). From 1 to 9 cycles, the cell is charged up to 4.70 V with a rate of C/25, keeping the voltage constant at 4.70 V for 5 hours, followed by a discharge mode with a rate of C/100. After these 9 cycles, the cell is charged and discharged with a rate of C/100 between 4.6 and 2.0 V.

During the first charge, $Na_{2+\delta}Mn_{2-\delta/2}(SO_4)_3$ delivers a capacity of 61 mAh/g that corresponds to the extraction of 1

mol of Na^+ per formula unit (Fig. 11). The reverse process of discharging yields a higher capacity (i.e. of 125 mAh/g) corresponding to 2 mole of inserted alkaline ions. The observed irreversibility of the first cycle does not allow specifying whether Li^+ or Na^+ ions are intercalated during the first discharge process. However, the alluaudite structure offers favorable crystallographic sites for uptake of extra-framework alkaline cations. This is in an agreement with a Rietveld refinement of the two sodium positions Na2 and Na3 (Table 2).

It is of importance that the charge capacities during next cycles tend to the discharge ones, the Columbic efficiency being around 85-90 % (Fig. 11). On subsequent cycling, the charge curve undergoes a continuous change in respect of the potential where alkaline ions are deintercalated: there is a smooth decrease in the potential from 4.65 to 4.45 V at a rate of C/25. The discharge curves also display some changes during cycling. In the course of the first discharge, the capacity is delivered at two distinct plateaus: at high-voltage plateau at 4.20 V there is an insertion of only 0.1 mol of alkaline ions per formula unit, while most of alkaline ions (i.e. 1.9 mol per formula unit) are intercalated at low-voltage plateau 2.65 V. The high-voltage plateau diminishes progressively on cycling and, after 9 cycles, the low-voltage plateau is observed only. The potential of the low-voltage plateau remains intact during cycling. The charge and discharge curves become steady-state after several cycles (Fig. 11).

To identify voltages of reversible alkaline intercalation, the charge and discharge of the cell is carried out between 2.0 and 4.6 V with a low rate of C/100 (Fig. 11). Both charge and discharge curves display well defined oxidation and reduction plateaus at 4.12 and 2.60 V, respectively. The capacities associated with charge and discharge processes are 143 mAh/g and 135 mAh/g, respectively. These capacity values indicate that 2.35 mol of alkaline ions are extracted from formula unit $Na_{2.44}Mn_{1.78}(SO_4)_3$, while 2.23 mol of alkaline ions are inserted. The oxidation and reduction peaks can be attributed to the Mn^{2+}/Mn^{3+} redox couple in the alluaudite phase. For the sake of comparison, the same Mn^{2+}/Mn^{3+} redox couple is responsible for intercalation properties of the well known lithium manganese phospho-olivine $LiMnPO_4$: the reversible oxidation and reduction of manganese ions proceeds at 4.3 and 3.9 V, respectively.[14-16] The comparison shows that the oxidation of Mn^{2+} to Mn^{3+} in both olivine and alluaudite phases takes place above 4.0 V, while the reverse reduction reaction is proceeding at a significantly lower potential for the alluaudite phase. It is worth mentioning that the unstable discharge plateau at 4.2 V, observed only in the course of first several cycles, can be related with that for $LiMnPO_4$, thus giving evidence for Li^+ insertion into the alluaudite phase. Contrary to plateau at 4.2 V, the lower discharge plateau at 2.60 V cannot be explained on the basis of different electronic structure of Mn ions in the olivine and the alluaudite phases. This implies that Na^+ ions instead of Li^+ ones can be intercalated into the alluaudite phase. The insertion potential of Na^+ is lower, comparing with that of Li^+, due to the difference in the standard reduction potential for $Na^+(aq)/Na(s)$ and

Li$^+$(aq)/Li(s): -2.71 V versus -3.04 V and difference of 0.33 V. The potential difference, observed by us, is significantly higher than that of 0.33 V. It is noticeable that sodium manganese-iron phosphate NaMnFe$_2$(PO$_4$)$_3$ with an alluaudite-type of structure display a reduction of Fe/Mn^{3+} to Fe/Mn^{2+} at an average voltage around ~2.5 V, when it is used as a cathode in lithium cell versus Li anode.[5] At this level of examination, the mechanism of the electrochemical reaction remains unclear. However, our results demonstrate unambiguously that the alluaudite phase Na$_{2+\delta}$Mn$_{2-\delta/2}$(SO$_4$)$_3$ is electrochemically active, delivering a reversible capacity higher than that of lithium manganese phospho-olivine. In addition, the alluaudite phase Na$_{2+\delta}$Mn$_{2-\delta/2}$(SO$_4$)$_3$ is not covered with carbon additives, which is a usual procedure for LiMnPO$_4$ in order to achieve its good electrochemical performance.[3]

To rationalize the electrochemical behaviour of Na$_{2+\delta}$Mn$_{2-\delta/2}$(SO$_4$)$_3$ in lithium cells, *ex-situ* IR, Raman and EPR experiments have been undertaken. Figure 10 compares the IR and Raman spectra of the pristine composition and the electrode composition obtained after 25 cycles between 4.7 and 2.0 V. The IR spectra of PVDF and pyrrolidone (used as bonding and dispersing agents in the electrode fabrication) are also shown. The comparison shows that the IR spectrum of the electrode composition is not affected by the presence of PVDF and pyrrolidone agents only in the range where v_4-vibrations of SO$_4$ groups appear. In this range, the electrode composition displays the IR bands that match the positions and intensities of IR bands of SO$_4$ groups in the pristine composition.

The presence of carbon additives in the electrode composite is clearly detected by Raman spectroscopy (Fig. 10). The Raman spectra are dominated by two intensive bands at 1335 and 1595 cm^{-1}. These two bands are considered as fingerprints of disordered carbon with graphite-like medium-range order.[30-32] The band at 1595 cm^{-1} (denoted as G band) is due to the in-plane stretching motion of pair of sp^2 carbon atoms in aromatic and olefinic bonding.[30-33] The band at 1335 cm^{-1} (denoted as D band) is attributed to disorder-allowed phonon modes which become Raman active as a result of the disrupted symmetry of the graphite sheets (scattering from defects).[33] In addition to the G and D bands, the Raman spectrum of the electrode composition exhibits one low-intensity band at 1012 cm^{-1} with a slight asymmetry at the low wave-number side. The band position and its asymmetry coincide well with that for the v_1 mode of SO$_4$ groups in the pristine composition. The v_1 band in the electrode composition is much weaker than that in the pristine composition, which can be related to a screening effect of the carbon in the electrode composition. The results obtained from IR and Raman spectroscopy reveals that SO$_4$ network remains intact after the electrochemical reaction.

EPR spectroscopy allows monitoring the changes in the oxidation state of manganese ions after electrochemical reaction. As in the case of the pristine composition, the EPR spectrum of the electrode composition consists of single Lorentzian line (not shown). After the electrochemical reaction, the EPR signal is broader and it possesses lower *g*-factor in comparison with that of the signal of the pristine

composition (Fig. 9). On cooling down from 300 to 100 K, the *g*-factor shows a tendency to decrease, while the line width increases (Fig. 9). Although the *g*-value of the electrode composition falls within the typical range for Mn^{2+} ions, the slight temperature dependence of the g-factor suggests that the EPR signal is associated with a complex spin system rather than to exchange-coupled Mn^{2+} ions. This can be explained, if we suppose that highly oxidized Mn ions appear together with Mn^{2+} ions and all these manganese ions contribute to the broad signal. Taking into account the charging-discharging curves (Fig. 11), the redox couple Mn^{2+}/Mn^{3+} is responsible for the alkaline ion intercalation in Na$_{2+\delta}$Mn$_{2-\delta/2}$(SO$_4$)$_3$. In contrast to Mn^{2+} ions, the Mn^{3+} ions are unlikely to be detectable by EPR in the X-band region (i.e. at 9.4 GHz) due to their strong spin-lattice relaxation and large zero-field splitting parameters. However, their effect on the EPR response of Mn^{2+} ions is easily observable. The same picture has been observed for several layered and spinel oxides (such as delithiated lithium nickel manganese oxides, sodium deficient manganese oxides), where Mn^{3+} and Mn^{4+} coexist.[34] (It should be reminded that both Mn^{2+} and Mn^{4+} are to be observed easily by X-band EPR even at room temperature.) Therefore, the EPR signal of the electrode composition is assigned to Mn^{2+} ions, whose parameters are perturbed by Mn^{3+} ions. This is supported by the temperature dependence of the signal intensity: between 100 and 300 K, the signal intensity is changing following the Curie-Weiss law with a Weiss constant of -138 $\pm$ 9 K. The absolute value of the Weiss constant is higher in comparison with that for the pristine composition (i.e. -56 $\pm$ 7 K). On the one hand; the EPR signal is related to irreversibility of the electrochemical reaction, as a result of which Mn^{3+} ions appear in addition to Mn^{2+} ones. On the other hand, this is a direct spectroscopic evidence for oxidation and reduction of manganese ions during the electrochemical reaction.

Conclusions

Thermal decomposition of the kröhnkite phase Na$_2$Mn(SO$_4$)$_2$·2H$_2$O proceeds by a consecutive loss of the first and second H$_2$O molecule in the temperature range of 135 – 290 ^{o}C. The dehydration process is accompanied with a phase separation manifested by the splitting of the coordination of Mn^{2+} ions. Above 200 ^{o}C, an anhydrous phase with an alluaudite type structure and composition Na$_{2+\delta}$Mn$_{2-\delta/2}$(SO$_4$)$_3$ is formed. The change in the Na-to-Mn ratio during the dehydration process is a consequence of the fast Na$^+$ mobility into cavities of both kröhnkite and alluaudite phases. From structural point of view, the release of two H$_2$O molecule from the kröhnkite phase takes place by a transformation of the infinite [Mn(SO$_4$)$_2$(H$_2$O)$_2$] chains into Mn$_2$O$_{10}$ dimers bounded by distorted Na(1)O-polyhedra. The formation of the alluaudite phase by dehydration of the kröhnkite phase represents a new and simple synthetic route for the preparation of manganese-based polyanion electrode materials.

The alluaudite structure exhibits channels along *c* axis, whose effective pore sizes are very suitable for fast Na$^+$

mobility. This structural feature makes the alluaudite phase very attractive as electrode materials for rechargeable alkaline ion batteries. The anhydrous sulfates are able to participate in the electrochemical reaction delivering reversible capacity of 135 mAh/g, when they are used as cathode materials in lithium ion cells. Prior to the electrochemical test, it is demonstrated that $Na_{2+\delta}Mn_{2-\delta/2}(SO_4)_3$ is stable in the lithium electrolyte containing 1M $LiPF_6$ solution in ethylene carbonate and in dimethyl carbonate. In a lithium cell versus Li anode, the alluaudite phase $Na_{2+\delta}Mn_{2-\delta/2}(SO_4)_3$ is able to intercalate reversibly of around 2.2 mol alkaline ions. The SO_4 network remains intact during the electrochemical reaction. The reversible intercalation of Li^+ and Na^+ takes place at two distinct voltage plateaus (i.e. 4.12 and 2.60 V) owing to the redox Mn^{2+}/Mn^{3+} couple. The good electrochemical performance is achieved after several "activation" cycles including a progressive shift of the oxidation plateau down to 4.12 V and disappearance of the reduction plateau at 4.2 V. The reduction plateau at 2.60 V is stable during cycling.

As far as we know, this is the first experimental report on the electrochemical activity of sodium manganese sulfates with an alluaudite-type of structure. Although the electrochemical performance of $Na_{2+\delta}Mn_{2-\delta/2}(SO_4)_3$ is not yet optimized, these first studies could give impetus for further investigations of electrochemical properties of manganese-based sulfates in both lithium- and sodium-ion batteries. Moreover, the alluaudite phase $Na_{2+\delta}Mn_{2-\delta/2}(SO_4)_3$ displays, even in this unoptimized state, a better electrochemical performance in comparison with that of well-known lithium manganese phospho-olivine $LiMnPO_4$.

References

1   C. Masquelier and L. Croguennec, *Chem. Rev*, 2013, **113**, 6552.
2   A.K. Padhi, K.S. Nanjuindaswamy and J.B. Goodenough, *J. Electrochem. Soc.,* 1997, **144**, 1188.
3   Z. Gong and Yong Yang, *Energy Environ. Sci.*, 2011, **4**, 3223.
4   T.J. Richardson, *J. Power Sources*, 2003, **119-121**, 262.
5   K. Trad, D. Carlier, L. Croguennec, A. Wattiaux, M. Ben Amara and C. Delmas, *Chem. Mater.* 2010, **22**, 5554.
6   P. Barpanda, G. Oyama, S. Nishimura, S.-C. Chung and A. Yamada, *Nature Commun.* 2014 DOI: 10.1038/ncomms5358.
7   L.L. Wong, H.M. Chen and S. Adams, *Phys. Chem. Chem. Phys.* 2015, **17,** 9186.
8   D. Dwibedi, R.B. Araujo, S. Chakraborty, P.P. Shanbogh, N.G. Sundaram, R. Ahuja, P. Barpanda, *J. Mater. Chem. A,* 2015, DOI: 10.1039/C5TA04527D.
9   D. Fisher, *J. Am. Mineral.* 1955, **40**, 1100.
10 P.B. Moore, *J. Am. Mineral.* 1971, **56**, 1955.
11 H. Ehrenberga, E. Muessig, K.G. Bramnik, P. Kampe and T. Hansen, *Solid State Sciences* 2006, **8**, 813.
12 N. Yabuuchi, K. Kubota, M. Dahbi, S. Komaba, *Chem. Rev.,* 2014, **114,** 11636.
13 B.L. Ellis and L.F. Nazar, *Curr. Opin. Solid State Mater. Sci.* 2012, **16**, 168.
14 J.M. Clark, C. Eames, M. Reynaud, G. Rousse, J.-N. Chotard, J.-M. Tarascon, M. Saiful Islam, *J. Mater. Chem. A* 2014, **2**, 7446.
15 P. Barpanda, G. Oyama, C.D. Ling and A. Yamada, *Chem. Mater.* 2014, **26**, 1297.
16 Y. Meng, S. Zhang and C. Deng, *J. Mater. Chem. A* 2015, **3**, 4484.
17 D. Choi, D. Wang, I.-T. Bae, J. Xiao, Z. Nie, W. Wang, V.V. Viswanathan, Y.J. Lee, J.-G. Zhang, G.L. Graff, Z. Yang and J. Liu, *Nano Lett.* 2010, **10**, 2799.
18 C. Delacourt, L. Laffont, R. Bouchet, C. Wurm, J.-B. Leriche, M. Morcrette, J.-M. Tarascon and C.J. Masquelier, *J. Electrochem. Soc.* 2005, **152**, A913.
19 A. Morgan, A. Van der Ven, G. Ceder, *Electrochem. Solid-State Lett.* 2004, **7**, A30.
20 W.F. Linke, Solubilities of inorganic and metal organic compounds, *Am. Chem. Soc.* 1965, 2, 566.
21 A.C. Larson, R.B. Von Dreele, General Structure Analysis System (GSAS), Report LAUR 86-748, Los Alamos National Laboratory, (2000).
22 B.H. Toby, EXPGUI, a graphical user interface for GSAS. *J. Appl. Crystallogr.* 2001, **34**, 210.
23 International Centre for Diffraction Data ICDD 4.14.0.6 using PDF-4+ 2014 RDB 4.
24 M. Wildner and D. Stoilova, *Z. Kristallogr.* 2003, **218**, 201.
25 M. Fleck, U. Kolitsch, B. Hertweck, *Z. Kristallogr.* 2002, **217**, 435.
26 D. Swain and T.N. Guru Row, *Inorg. Chem.* 2009, **48**, 7048.
27 Nakamoto, K., Infrared spectra of inorganic and coordination compounds, Izd. Mir., 1966, Moscow.
28 V. Ivanovsky, V.M. Petrusevski, B. Shoptrajanov, *Vibr. Spec.*, 1999, **19**, 425.
29 K. Xu, *Chem. Rev.*, 2004, **104**, 4303.
30 Y. Liu, C. Pan, J. Wang, *J. Mater. Sci.,* 2004, **39**, 1091.
31 F. Tuinstra and J.L. Koenig, *J. Chem. Phys.*, 1970, **53**, 1126.
32 J. Robertson, *J Non Cryst Solids,* 2002, **299–302**, 798.
33 A.C. Ferrari and J. Robertson, *Phys. Rev. B*, 2000, **61**, 14095.
34 (a) R. Stoyanova, E. Zhecheva and S. Vassilev, *J. Solid State Chem.*, 2006, **179**, 378; (b) R. Stoyanova, D. Carlier, M. Sendova-Vassileva, M. Yoncheva, E. Zhecheva, D. Nihtianova, C. Delmas, *J. Solid State Chem.,* 2010, **183**, 1372; (c) R. Stoyanova, E. Zhecheva, R. Alcántara and J.L. Tirado, *J. Mater. Chem.*, 2006, **16**, 359.

Graphical Abstract

From kröhnkite- to alluaudite-type of structure: novel method of synthesis of sodium manganese sulfates with electrochemical properties in alkaline ion batteries

D. Marinova,[a] V. Kostov,[b] R. Nikolova,[b] R. Kukeva,[a] E. Zhecheva,[a] M. Sendova-Vasileva,[c] and R. Stoyanova[a]*

Well-crystallized sodium manganese sulfates $Na_{2+\delta}Mn_{2-\delta/2}(SO_4)_3$ with an alluaudite-type of structure is obtained by dehydration of the kröhnkite-type phase $Na_2Mn(SO_4)_3 \cdot 2H_2O$. The alluaudite-phases are able to participate in the electrochemical reaction delivering reversible capacity of 135 mAh/g, when they are used as cathode materials in lithium ion cells.